

# Enabling Solar Water Oxidation by BiVO<sub>4</sub> in Strongly Acidic Solutions

Daye Seo,<sup>§</sup> Dae Han Wi,<sup>§</sup> and Kyoung-Shin Choi\*



Cite This: <https://doi.org/10.1021/jacs.5c11785>



Read Online

ACCESS |



Metrics & More

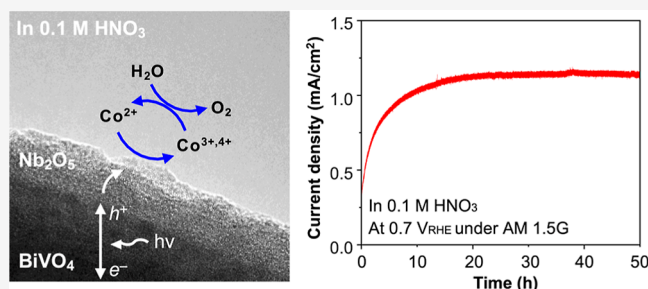


Article Recommendations



Supporting Information

**ABSTRACT:** The oxygen evolution reaction (OER) is paired with various electrochemical and photoelectrochemical reduction reactions used for fuel and chemical production. As there is a strong interest in performing many of these reduction reactions in strongly acidic solutions to increase the reaction rate, efficiency, or selectivity, there is also a great interest in enabling efficient and stable OER in strongly acidic solutions. In this study, we report stable photoelectrochemical OER (POER) of a BiVO<sub>4</sub> photoanode in 0.1 M HNO<sub>3</sub> (pH 1). This was achieved by using Nb<sub>2</sub>O<sub>5</sub> as a protection layer. While Nb<sub>2</sub>O<sub>5</sub> was rarely used as a protection layer for photoelectrodes in the past, we show its excellent capability to suppress both the chemical and photoelectrochemical dissolution of BiVO<sub>4</sub> at pH 1. After stabilizing BiVO<sub>4</sub> with a Nb<sub>2</sub>O<sub>5</sub> protection layer, we added Co<sup>2+</sup> ions to the electrolyte as an OER catalyst to enhance the POER. We found that Co<sub>(aq)</sub><sup>2+</sup> can serve as a homogeneous OER catalyst without being deposited as a CoO<sub>x</sub> solid catalyst on Nb<sub>2</sub>O<sub>5</sub>. When we performed the POER using unprotected BiVO<sub>4</sub> with Co<sub>(aq)</sub><sup>2+</sup> under the same condition, although POER was enhanced, the enhancement could not be sustained due to the chemical dissolution of BiVO<sub>4</sub>. After the POER, we found that a Co<sup>3+</sup>-containing OER catalyst was deposited on the bare BiVO<sub>4</sub> surface. This result suggested that the use of Co<sup>2+</sup> ions as a homogeneous catalyst was possible due to the inertness of the Nb<sub>2</sub>O<sub>5</sub> surface toward the adsorption or deposition of Co ions. This study enabling stable POER of BiVO<sub>4</sub> in 0.1 M HNO<sub>3</sub> using the combination of a Nb<sub>2</sub>O<sub>5</sub> protection layer and Co<sub>(aq)</sub><sup>2+</sup> as a homogeneous OER catalyst provides promising possibilities for acidic POER and OER.



## INTRODUCTION

The oxygen evolution reaction (OER) is the most convenient and environmentally benign anode reaction to be coupled with various cathode reactions that produce fuels and chemicals in aqueous media, which include the hydrogen evolution reaction (HER), nitrogen or nitrate reduction, CO<sub>2</sub> reduction reaction (CO<sub>2</sub>RR), and organic reduction including hydrogenation and hydrogenolysis.<sup>1–4</sup> There are various advantages to performing many of these cathode reactions in acidic solutions. For example, the kinetics of most HER catalysts are known to be faster in acidic solutions.<sup>5,6</sup> CO<sub>2</sub>RR in acidic solutions has the advantage of preventing the conversion of CO<sub>2</sub> to bicarbonate or carbonate, thus allowing for more efficient CO<sub>2</sub> reduction.<sup>7,8</sup> Furthermore, recent studies reported that electrochemical hydrodeoxygenation reactions of biomass-derived oxygenates, which are critical to produce biofuels, are enhanced in acidic solutions.<sup>9,10</sup>

When the aforementioned cathode reactions are performed in acidic solutions, the paired OER in the same acidic solutions can create multiple issues. For example, the OER kinetics are reported to be more sluggish in acidic solutions than in alkaline solutions, in contrast to the HER kinetics.<sup>11</sup> In addition, catalyst stability is another significant challenge for acidic OER; under the combination of strong acidity and anodic bias

required for the OER, most nonprecious metal OER catalysts are not stable over long-term use.<sup>12,13</sup> Thus, there is a critical need for developing inexpensive OER catalysts that are efficient and stable in acidic solutions.

The photoelectrochemical OER (POER) may offer a unique advantage to circumvent the challenges associated with the sluggish kinetics of the OER.<sup>14</sup> This is because the POER is achieved by holes in the valence band (VB) of a photoanode (i.e., n-type semiconductor), which are generated through photon absorption that excites electrons from the VB to the conduction band (CB). If a photoanode has a valence band maximum (VBM) significantly more positive than 1.23 V vs reversible hydrogen electrode (RHE), the holes at the VBM will have a sufficient overpotential for the OER, without requiring additional electrical bias. Another advantage is that the photoexcited electrons at the conduction band minimum

Received: July 11, 2025

Revised: August 24, 2025

Accepted: September 4, 2025

(CBM) of the photoanode will be transferred to the cathode to perform the aforementioned reduction reactions. Since the potential of photoexcited electrons is elevated to that of the CBM of the photoanode, additional electrical bias needed to conduct the desired reduction reaction can be significantly reduced, if the CBM of the photoanode is near or above 0 V vs RHE. Thus, the use of the POER may be particularly beneficial if the operating voltage required to conduct the desired cathode reaction paired with the OER is considerably high (>2 V).

Considering the energetic requirements of the photoanode to meet these criteria, n-type BiVO<sub>4</sub> is a particularly attractive photoanode. Its VBM is 2.4 V vs RHE, providing more than 1 V of overpotential for the OER, and its CBM is near 0 V vs RHE.<sup>15</sup> Also, its bandgap (~2.4 eV) allows for visible light utilization.<sup>15</sup> However, in order to use BiVO<sub>4</sub> as a photoanode for the POER in acidic solutions, two critical issues need to be addressed. First, while BiVO<sub>4</sub> is shown to perform the OER stably in near neutral solutions,<sup>16–18</sup> BiVO<sub>4</sub> is not chemically stable in acidic solutions. Thus, BiVO<sub>4</sub> will require a protection layer to prevent dissolution. Unfortunately, while TiO<sub>2</sub>, the most commonly used protection layer for various photoelectrodes, has been used to protect BiVO<sub>4</sub> in mildly basic solutions successfully,<sup>19,20</sup> TiO<sub>2</sub> as a thin amorphous protection layer appears to be not robust enough to protect BiVO<sub>4</sub> in strongly acidic media, supported by no studies reporting the use of TiO<sub>2</sub>-protected BiVO<sub>4</sub> in strongly acidic solutions (pH < 2). Thus, the identification of a material that can serve as a more robust protection layer in strongly acidic solutions and a method to deposit this material as a conformal protection layer will be needed. Second, while the holes in BiVO<sub>4</sub> have sufficient overpotential for the OER, the surface of BiVO<sub>4</sub> is not catalytic for the OER. Thus, there is still a need to identify stable, efficient, and inexpensive OER catalysts that can best utilize highly oxidizing holes generated in BiVO<sub>4</sub> for the POER in strongly acidic solutions.

In this study, we present stable POER of BiVO<sub>4</sub> in 0.1 M HNO<sub>3</sub> (pH 1), which is enabled by using Nb<sub>2</sub>O<sub>5</sub> as a protection layer and Co<sup>2+</sup> as a homogeneous OER catalyst. We report an electrodeposition method to form a conformal coating of Nb<sub>2</sub>O<sub>5</sub> on a nanoporous BiVO<sub>4</sub> photoanode having a complex surface morphology and show the capability of Nb<sub>2</sub>O<sub>5</sub> to protect BiVO<sub>4</sub> from chemical and photoelectrochemical corrosion. We also show that Co<sup>2+</sup> ions can serve as a homogeneous OER catalyst on a Nb<sub>2</sub>O<sub>5</sub>-protected BiVO<sub>4</sub> photoanode, which eliminates not only the need to predeposit the catalyst on Nb<sub>2</sub>O<sub>5</sub> but also the concerns related to the dissolution loss of the catalyst during the OER in acidic solutions. Our investigation on the unprecedented combination of a Nb<sub>2</sub>O<sub>5</sub> protection layer and Co<sup>2+</sup> as a homogeneous OER catalyst offers strategies that may be extended to enhance chemical and photoelectrochemical stabilities of other photoelectrodes.

## EXPERIMENTAL SECTION

**Materials.** Bismuth(III) nitrate pentahydrate (Bi(NO<sub>3</sub>)<sub>3</sub>·5H<sub>2</sub>O, 98%), potassium iodide (KI, 99+%), nitric acid (HNO<sub>3</sub>, 70% and 0.1 M), ammonium niobate(V) oxalate hydrate (NH<sub>4</sub>[NbO(C<sub>2</sub>O<sub>4</sub>)<sub>2</sub>]·xH<sub>2</sub>O, 99.99%), *p*-benzoquinone (*p*-BQ, >98%), vanadium acetylacetonate (VO(C<sub>5</sub>H<sub>7</sub>O<sub>2</sub>)<sub>2</sub>, 98%), sodium hydroxide (NaOH, >97%), cobalt(II) nitrate hexahydrate (Co(NO<sub>3</sub>)<sub>2</sub>·6H<sub>2</sub>O, >98%), sodium sulfite (Na<sub>2</sub>SO<sub>3</sub>, >98%), boric acid (H<sub>3</sub>BO<sub>3</sub>, >99.5%) and isopropanol (IPA, 99.9%) were purchased from Sigma-Aldrich. Dimethyl sulfoxide (DMSO, 99.9%) and lactic acid (85%) were purchased from Alfa

Aesar Chemicals. Ethanol (200 proof) was purchased from Decon Laboratories. All chemicals were used as purchased without further purification. The deionized water (DI water, >18 MΩ·cm) used in this study was prepared by the Barnstead E-Pure water purification system. Glass substrates coated with fluorine-doped tin oxide (FTO) were purchased from Hartford Glass Co. Nafion membranes (N211) were purchased from Fuel Cell Store.

**Preparation of BiVO<sub>4</sub>/Nb<sub>2</sub>O<sub>5</sub>.** Nanoporous BiVO<sub>4</sub> photoanodes were prepared following the method that our group developed previously,<sup>17</sup> which uses an electrodeposited BiOI film as a precursor to form a nanoporous BiVO<sub>4</sub> electrode. The plating solution for BiOI deposition was prepared by mixing four different solutions: (i) 50 mL of an aqueous solution containing 15 mM Bi(NO<sub>3</sub>)<sub>3</sub> and 400 mM KI, (ii) 20 mL of ethanol solution containing 46 mM of *p*-BQ, (iii) 169 μL of lactic acid (85%), and (iv) 120 μL of 10-fold-diluted 70% nitric acid. A three-electrode system with an FTO working electrode (WE), an FTO counter electrode (CE), and an Ag/AgCl (4 M KCl) reference electrode (RE) was employed for the electrodeposition. Before use, FTO electrodes were cleaned by sonicating in soapy water and isopropanol successively. For use as the WE, an FTO electrode was masked with PTFE tape such that the exposed area was 1 cm × 1.25 cm. An unmasked FTO electrode, whose size was ~1.5 × 1.8 cm<sup>2</sup>, was used as the CE. Two different potentials were sequentially applied to the FTO electrodes: (i) -0.33 V vs Ag/AgCl for 20 s to induce Bi nucleation and (ii) -0.1 V vs Ag/AgCl for BiOI growth through *p*-BQ reduction. The detailed deposition mechanisms can be found elsewhere.<sup>17</sup> The charge passed during the growth step was 0.35 C/cm<sup>2</sup>. As-deposited films were washed with DI water and dried under a stream of air. To convert the BiOI films into n-type BiVO<sub>4</sub>, 65 μL of a DMSO solution containing 200 mM VO(C<sub>5</sub>H<sub>7</sub>O<sub>2</sub>)<sub>2</sub> was dropcast onto the BiOI film, and then the film was annealed at 450 °C for 2 h (ramping rate: 2 °C/min) in air. After the thermal treatment, excess V<sub>2</sub>O<sub>5</sub> was removed by soaking the electrodes in a 1 M NaOH solution for 15 min. BiVO<sub>4</sub> photoanodes were annealed in N<sub>2</sub> conditions for another 2 h at 350 °C (ramping rate: 5 °C/min) to further enhance their photocurrent generation.<sup>21</sup>

The Nb<sub>2</sub>O<sub>5</sub> protection layer was electrochemically deposited on nanoporous BiVO<sub>4</sub> using the same *p*-BQ reduction. The detailed deposition mechanism is explained below. The electrodeposition used a three-electrode setup composed of a nanoporous BiVO<sub>4</sub> photoanode as the WE, an FTO CE, and an Ag/AgCl (4 M KCl) RE. The electroplating solution was composed of DMSO and DI water with the 3:2 (v/v) ratio, which contained 10 mM NH<sub>4</sub>[NbO(C<sub>2</sub>O<sub>4</sub>)<sub>2</sub>]·xH<sub>2</sub>O and 100 mM *p*-BQ. The Nb precursor and *p*-BQ were fully dissolved in DMSO first and then DI water was added. The reported concentrations of Nb precursor and *p*-BQ are final concentrations after the DI water is added. The electrodeposition was carried out at -0.6 V vs Ag/AgCl for 10 min. During the deposition, the electrolyte temperature was maintained at 85 °C using an oil bath. The average current density during the deposition process was -2.5 mA/cm<sup>2</sup>.

As-prepared electrodes were washed with ethanol and dried with a gentle steam of air. To dehydrate the NbO<sub>x</sub>(OH)<sub>y</sub> layer, thermal treatment was conducted at 350 °C for 2 h (ramping rate: 3.5 °C/min) under a N<sub>2</sub> environment (flow rate: 10 ccm). These synthesis conditions resulted in the deposition of a 10–15 nm-thick Nb<sub>2</sub>O<sub>5</sub> layer on BiVO<sub>4</sub>. Deposition of a thinner or thicker Nb<sub>2</sub>O<sub>5</sub> layer is possible by adjusting the deposition potential or time. For example, a thinner Nb<sub>2</sub>O<sub>5</sub> layer (e.g., ~5 nm thick) could be deposited on BiVO<sub>4</sub> when the electrodeposition potential and time were adjusted to -0.2 V and 5 min (average current density = -1.2 mA/cm<sup>2</sup>), respectively (Figure S1a). However, decreasing the thickness of the Nb<sub>2</sub>O<sub>5</sub> layer did not result in an increase in photocurrent of the resulting BiVO<sub>4</sub>/Nb<sub>2</sub>O<sub>5</sub> photoanode (Figure S1b), suggesting that there is no gain for decreasing the thickness of the Nb<sub>2</sub>O<sub>5</sub> layer below 10–15 nm.

**Materials Characterization.** X-ray diffraction (XRD) patterns of the samples were obtained using an X-ray diffractometer (Bruker D8 Discover) with a Cu Kα (λ = 1.54178 Å) radiation source. Scanning electron microscopy (SEM) images of the samples were acquired using a scanning electron microscope (Zeiss Supra VP55). Transmission electron microscopy (TEM) images, high-angle annular dark-

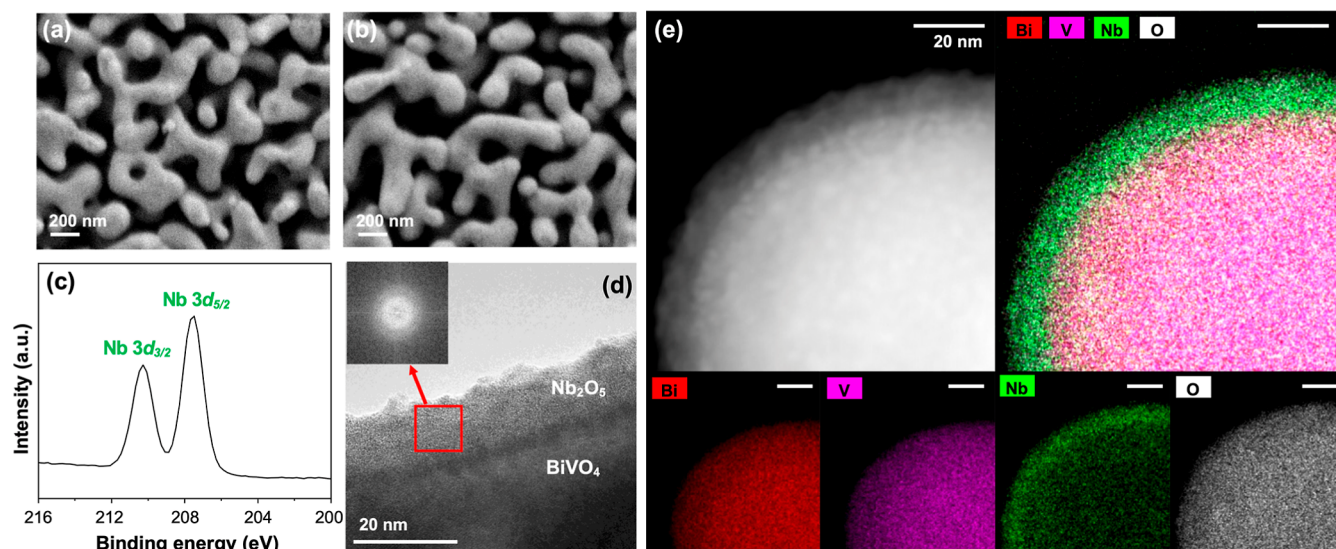


**Figure 1.** Characterization of BiVO<sub>4</sub>/Nb<sub>2</sub>O<sub>5</sub>. SEM images of (a) bare BiVO<sub>4</sub> and (b) BiVO<sub>4</sub>/Nb<sub>2</sub>O<sub>5</sub> photoanodes. (c) Nb 3d XPS spectrum of BiVO<sub>4</sub>/Nb<sub>2</sub>O<sub>5</sub>. (d) A representative TEM image of BiVO<sub>4</sub>/Nb<sub>2</sub>O<sub>5</sub> with an inset showing the FFT of the Nb<sub>2</sub>O<sub>5</sub> region. (e) HAADF-STEM image and corresponding EDS element mapping images of BiVO<sub>4</sub>/Nb<sub>2</sub>O<sub>5</sub>. All scale bars in (e) are 20 nm.

field scanning transmission electron microscopy (HAADF-STEM) images and corresponding energy dispersive X-ray spectroscopy (EDS) mapping images were obtained using FEI Tecnai G2 F30 S-TWIN and Talos F200X transmission electron microscope operating at 200 kV. X-ray photoelectron spectroscopy (XPS) spectra were obtained using an X-ray photoelectron spectrometer (Thermo K-Alpha X-ray photoelectron spectrometer) with Al K $\alpha$  X-ray source. For the calibration of the XPS data, the C 1s peak at 284.8 eV was used as a reference. For the evaluation of chemical stability of BiVO<sub>4</sub> and BiVO<sub>4</sub>/Nb<sub>2</sub>O<sub>5</sub> photoanodes, the photoanodes were immersed in 0.1 HNO<sub>3</sub> (10 mL) for 3 weeks and their stabilities were periodically monitored using SEM and XRD.

**Photoelectrochemical Investigation.** All photoelectrochemical measurements were conducted with an SP-200 potentiostat (Bio-Logic Science Instrument). Solar illumination was simulated using an LCS-100 solar simulator (Oriel Instruments) equipped with a 100 W Xe arc lamp (Newport) and an AM 1.5G filter. An infrared filter (Newport) and a focusing lens (Newport) were placed between the light source and the photoelectrode. As back-side illumination was used, the light intensity was calibrated to 100 mW/cm<sup>2</sup> at the back side of the photoelectrode (i.e., at the FTO surface before the light enters the FTO electrode) using an NREL-certified GaAs reference cell (PV Measurements). The entire area of the BiVO<sub>4</sub> electrode (~1.25 cm<sup>2</sup>) was illuminated. A homemade closed quartz cell with a flat window for illumination was utilized. The cells were divided into anodic and cathodic chambers with a glass frit (pore size: 4–8  $\mu$ m, Ace Glass). Typically, each chamber was filled with 15 mL of solutions for photoelectrochemical measurements. A three-electrode setup composed of a BiVO<sub>4</sub> photoanode WE, a Pt plate CE, and a Ag/AgCl (4 M KCl) RE was used. The WE and RE were immersed in the anodic chamber while the CE was immersed in the cathodic chamber.

The photoelectrochemical water oxidation was conducted in 0.1 M HNO<sub>3</sub> (pH 1). When CoO<sub>2</sub><sup>+</sup> was utilized as an OER catalyst, 20 mM of Co(NO<sub>3</sub>)<sub>2</sub>·6H<sub>2</sub>O was added to the solution. The *J*–*V* plots were obtained under chopped illumination to measure the dark current and photocurrent densities during a single potential scan. The potential was scanned from the open circuit potential to the positive direction with a scan rate of 10 mV/s. The *J*–*t* plots were measured at 0.7 V vs RHE. All water oxidation results in this work are presented with respect to RHE for easy comparison with other reports using various pH conditions unless otherwise specified. Potentials versus Ag/AgCl (4 M KCl) reference electrodes ( $E_{(vs\ Ag/AgCl)}$ ) were converted to potentials versus RHE ( $E_{(vs\ RHE)}$ ) using eq 1.

$$E_{(vs\ RHE)} = E_{(vs\ Ag/AgCl)} + E_{Ag/AgCl(4\ M\ KCl)} + (0.0591\ V \times pH) \quad (1)$$

where  $E_{Ag/AgCl(4\ M\ KCl)} = 0.1976\ V$  vs SHE at 25 °C.

O<sub>2</sub> measurement was performed using a gastight closed cell with a Nafion membrane dividing the cathode and anode compartments. The volume of the head space in the anodic chamber was 24 mL and the O<sub>2</sub> gas was detected using an Ocean Optics fluorescence-based oxygen sensor (Neofox, FOSPOR-R). The probe was inserted into the headspace of the anodic chamber, and the vol % of evolved O<sub>2</sub> was continuously recorded. The measurement was performed while a constant potential of 0.7 V vs RHE was applied to BiVO<sub>4</sub>/Nb<sub>2</sub>O<sub>5</sub> (1.25 cm<sup>2</sup>) under illumination. The Faradaic efficiency (FE) was calculated by dividing the amount of gas detected by the theoretical amount of gas calculated on the basis of the total charge passed, using the following equation

$$FE\ (\%) = \frac{4 \times n\ (\text{mol}) \times F\ (\text{C mol}^{-1})}{\text{charge passed (C)}} \times 100\ (\%) \quad (2)$$

where *n* is moles of evolved O<sub>2</sub> gas and *F* is the Faraday constant (96,485.33 C mol<sup>-1</sup>).

## RESULTS AND DISCUSSION

**Electrodeposition of Nb<sub>2</sub>O<sub>5</sub> on BiVO<sub>4</sub>.** In this study, we used Nb<sub>2</sub>O<sub>5</sub> as a protection layer to operate high surface area, nanoporous BiVO<sub>4</sub> photoanodes<sup>16,17</sup> for POER in strongly acidic solutions. Nb<sub>2</sub>O<sub>5</sub> was chosen as it is one of the few oxides that are chemically stable in strongly acidic solutions across a wide potential range,<sup>22</sup> but has rarely been explored as a protection layer for semiconductor photoelectrodes.<sup>23</sup> In order to form a thin conformal Nb<sub>2</sub>O<sub>5</sub> layer on BiVO<sub>4</sub>, we electrodeposited Nb<sub>2</sub>O<sub>5</sub> using the nanoporous BiVO<sub>4</sub> electrode as the WE.

The water-soluble NH<sub>4</sub>[NbO(C<sub>2</sub>O<sub>4</sub>)<sub>2</sub>]·*x*H<sub>2</sub>O was used as the Nb precursor, and the electrodeposition of Nb<sub>2</sub>O<sub>5</sub> was achieved using the reduction of *p*-BQ to hydroquinone (eq 3). This reduction reaction consumes protons and increases the local pH on the BiVO<sub>4</sub> surface, which decreases the solubility of the Nb<sup>5+</sup> precursor, resulting in the precipitation of Nb<sub>2</sub>O<sub>5</sub> as NbO<sub>*x*</sub>(OH)<sub>*y*</sub>, the hydrated form of Nb<sub>2</sub>O<sub>5</sub>, coating the BiVO<sub>4</sub> surface. While there are other reduction reactions (e.g., HER

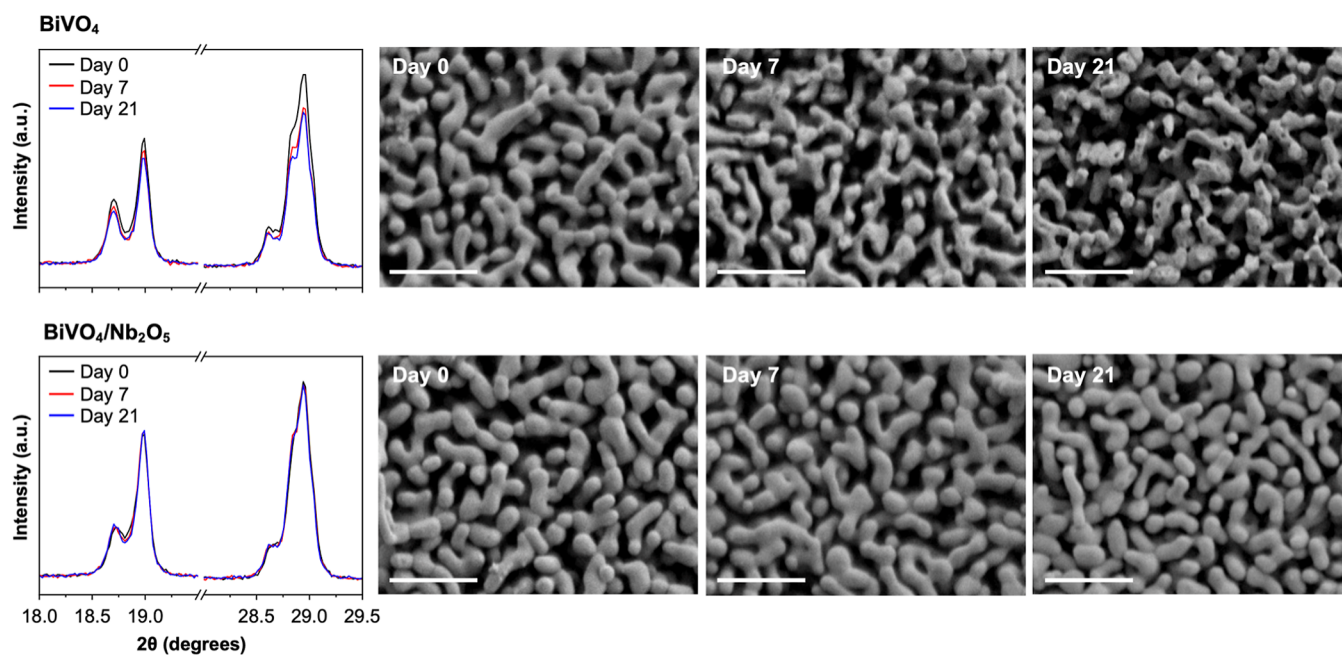
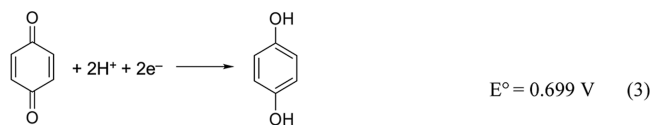


**Figure 2.** Effect of the Nb<sub>2</sub>O<sub>5</sub> layer on the chemical stability of BiVO<sub>4</sub> in 0.1 M HNO<sub>3</sub> (pH 1). XRD peaks (left) and SEM images (right) of bare BiVO<sub>4</sub> (top) and BiVO<sub>4</sub>/Nb<sub>2</sub>O<sub>5</sub> (bottom) measured before and after 7 and 21 days of immersion. Scale bars in the SEM images are 1 μm.

and nitrate reduction) that can consume H<sup>+</sup> or generate OH<sup>-</sup> to increase the local pH on the WE,<sup>24</sup> they are not viable when BiVO<sub>4</sub> or Bi<sup>3+</sup> containing material is used as the WE. This is because the thermodynamic potential and kinetic overpotential needed for these reduction reactions can reduce Bi<sup>3+</sup> in BiVO<sub>4</sub>, destroying the BiVO<sub>4</sub> electrode.<sup>19,25</sup> In contrast, the reduction of *p*-BQ can be achieved without changing the composition of the BiVO<sub>4</sub> WE. After the deposition, the NbO<sub>*x*</sub>(OH)<sub>*y*</sub> layer was dehydrated to Nb<sub>2</sub>O<sub>5</sub> by annealing at a mild condition (350 °C with N<sub>2</sub> for 2 h), resulting in the formation of Nb<sub>2</sub>O<sub>5</sub>-coated BiVO<sub>4</sub>, BiVO<sub>4</sub>/Nb<sub>2</sub>O<sub>5</sub>.



The SEM images of BiVO<sub>4</sub> and BiVO<sub>4</sub>/Nb<sub>2</sub>O<sub>5</sub> showed no noticeable difference (Figure 1a,b), confirming that the nanoporous structure of BiVO<sub>4</sub> remained intact during the electrodeposition of Nb<sub>2</sub>O<sub>5</sub>. Also, they suggested that Nb<sub>2</sub>O<sub>5</sub> was deposited as a thin layer with no distinguishable morphology. The presence of a thin, conformal Nb<sub>2</sub>O<sub>5</sub> layer on BiVO<sub>4</sub> was verified using multiple methods. First, Nb 3d XPS spectra showed the presence of Nb<sup>5+</sup> on the BiVO<sub>4</sub>/Nb<sub>2</sub>O<sub>5</sub> surface; the two characteristic peaks at 207.5 and 210.3 eV correspond to 3d<sub>5/2</sub> and 3d<sub>3/2</sub> peaks of Nb<sup>5+</sup> (Figure 1c). Second, the TEM image of BiVO<sub>4</sub>/Nb<sub>2</sub>O<sub>5</sub> showed that the Nb<sub>2</sub>O<sub>5</sub> layer was 10–15 nm thick (Figure 1d). The fast Fourier transform (FFT) of the Nb<sub>2</sub>O<sub>5</sub> region in the bright-field image revealed that the Nb<sub>2</sub>O<sub>5</sub> layer was amorphous (Figure 1d, inset), consistent with the XRD pattern of BiVO<sub>4</sub>/Nb<sub>2</sub>O<sub>5</sub> which did not show any Bragg peaks corresponding to crystalline Nb<sub>2</sub>O<sub>5</sub> (Figure S2). Lastly, the HAADF-STEM-EDS mapping additionally confirmed that the Nb<sub>2</sub>O<sub>5</sub> layer uniformly covered the BiVO<sub>4</sub> surface with no notable pinholes in the numerous specimens we examined (Figure 1e).

**Chemical Stability of BiVO<sub>4</sub>/Nb<sub>2</sub>O<sub>5</sub> at pH 1.** Before evaluating the effect of Nb<sub>2</sub>O<sub>5</sub> on the photoelectrochemical property and stability of BiVO<sub>4</sub>, we first examined the ability of Nb<sub>2</sub>O<sub>5</sub> to protect BiVO<sub>4</sub> from chemical dissolution in 0.1 M HNO<sub>3</sub> (pH 1) for 21 days of immersion. As unprotected BiVO<sub>4</sub> would dissolve in this solution, this test allows us to examine two things. First, a 10–15 nm thick, amorphous Nb<sub>2</sub>O<sub>5</sub> layer is stable and robust enough in 0.1 M HNO<sub>3</sub> to protect BiVO<sub>4</sub> from dissolution. Second, the Nb<sub>2</sub>O<sub>5</sub> layer is pinhole-free. If pinholes, not detected by the TEM study, indeed exist in the Nb<sub>2</sub>O<sub>5</sub> layer, BiVO<sub>4</sub> should dissolve gradually during the 3 weeks of the immersion time. We believe that this type of long-term immersion test offers the most rigorous method to verify the uniformity, conformality, and pinhole-free nature of the Nb<sub>2</sub>O<sub>5</sub> layer.

Figure 2 shows the comparison of XRD and SEM results of BiVO<sub>4</sub> and BiVO<sub>4</sub>/Nb<sub>2</sub>O<sub>5</sub> obtained before and after 7 and 21 days of immersion in 0.1 M HNO<sub>3</sub>. Not surprisingly, the loss of BiVO<sub>4</sub> by dissolution was evident after 7 days of immersion; the XRD results show a decrease in the BiVO<sub>4</sub> peaks and SEM images show the loss of BiVO<sub>4</sub>. For the case of BiVO<sub>4</sub>/Nb<sub>2</sub>O<sub>5</sub>, no noticeable changes in SEM images and XRD patterns were observed even after 21 days of immersion, confirming the absence of pinholes in the electrodeposited Nb<sub>2</sub>O<sub>5</sub> layer as well as the excellent stability of the electrodeposited Nb<sub>2</sub>O<sub>5</sub> coating on BiVO<sub>4</sub>.

**Photoelectrochemical Properties of BiVO<sub>4</sub>/Nb<sub>2</sub>O<sub>5</sub>.** Next, we compared the photoelectrochemical properties and stabilities of BiVO<sub>4</sub> and BiVO<sub>4</sub>/Nb<sub>2</sub>O<sub>5</sub> in 0.1 M HNO<sub>3</sub> under AM 1.5G illumination. It should be noted that protecting BiVO<sub>4</sub> against anodic photocorrosion is much more challenging than protecting BiVO<sub>4</sub> against chemical dissolution in the same acidic solution. This is because while the chemical dissolution of BiVO<sub>4</sub> caused by acid can be prevented by blocking the direct contact between BiVO<sub>4</sub> and acid by placing an acid-stable protection layer, the anodic photocorrosion of BiVO<sub>4</sub> is induced by surface-reaching photogenerated holes

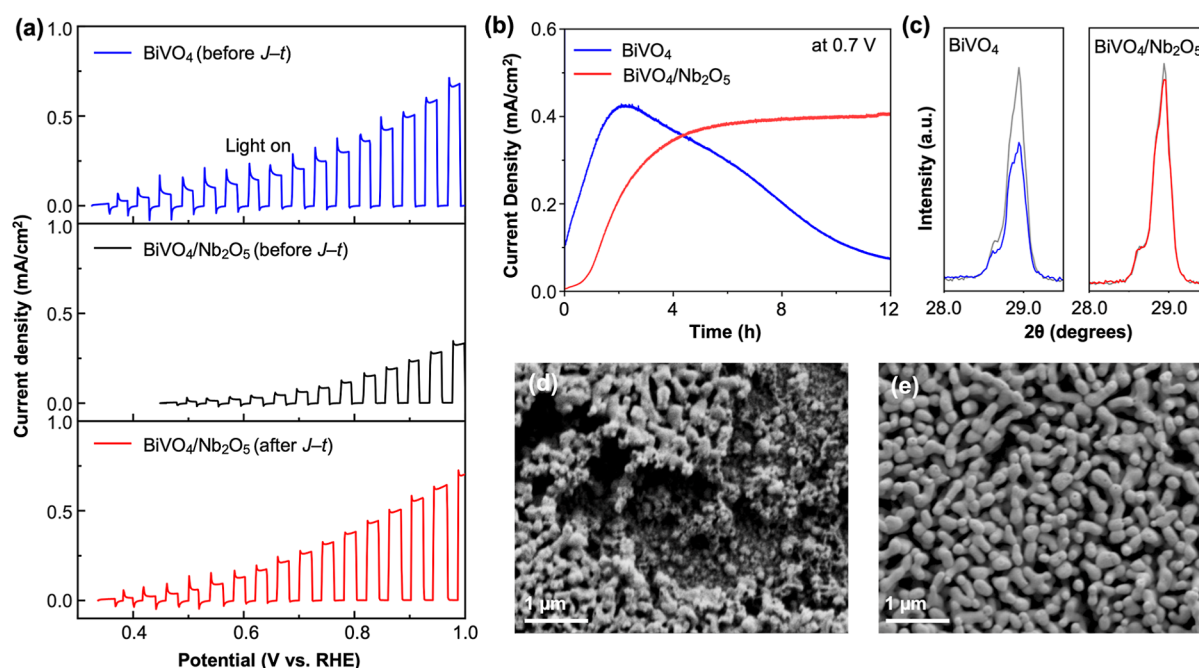


**Figure 3.** Effect of the  $\text{Nb}_2\text{O}_5$  layer on the photoelectrochemical stability of  $\text{BiVO}_4$  at pH 1. (a)  $J$ - $V$  plots of  $\text{BiVO}_4$  (blue) and  $\text{BiVO}_4/\text{Nb}_2\text{O}_5$  (black and red) measured in 0.1 M  $\text{HNO}_3$  under AM 1.5G illumination (scan rate: 10 mV/s). (b)  $J$ - $t$  plots of bare  $\text{BiVO}_4$  (blue) and  $\text{BiVO}_4/\text{Nb}_2\text{O}_5$  (red) at 0.7 V vs RHE. (c) XRD peak intensity change of  $\text{BiVO}_4$  (blue) and  $\text{BiVO}_4/\text{Nb}_2\text{O}_5$  (red) after the  $J$ - $t$  measurement. The most intense (112) peak of  $\text{BiVO}_4$  is shown as an example peak, and the gray line shows the peak of the pristine  $\text{BiVO}_4$ . SEM images of (d)  $\text{BiVO}_4$  and (e)  $\text{BiVO}_4/\text{Nb}_2\text{O}_5$  after the  $J$ - $t$  measurement.

within the  $\text{BiVO}_4$  underneath the protection layer. When the surface-reaching holes are not quickly consumed for water oxidation, the accumulated holes on the surface can oxidize  $\text{Bi}^{3+}$  or  $\text{O}^{2-}$  in the  $\text{BiVO}_4$  lattice. This anodic photocorrosion destroys the  $\text{BiVO}_4$  surface and weakens the  $\text{BiVO}_4$ /protection layer interface, allowing the acidic solution to reach the surface of  $\text{BiVO}_4$ , further accelerating the dissolution of  $\text{BiVO}_4$  by chemical and photoelectrochemical corrosion. Thus, a protection layer that can prevent the acidic dissolution can still fail to prevent anodic photocorrosion. In order for the protection layer to suppress photocorrosion, its composition and structure should be extremely robust such that it can hinder the interfacial atomic rearrangement on the  $\text{BiVO}_4$  surface that needs to be coupled for the photooxidation of  $\text{BiVO}_4$ . If the interfacial atomic rearrangement is difficult to occur, it can effectively slow down the rate of photocorrosion relative to the rates of surface recombination and the OER, allowing the surface holes to be consumed for surface recombination and OER instead, thereby preventing photocorrosion.

The comparison of the  $J$ - $V$  plots of  $\text{BiVO}_4$  and  $\text{BiVO}_4/\text{Nb}_2\text{O}_5$  photoanodes for the POER in 0.1 M  $\text{HNO}_3$  is shown in Figure 3a.  $\text{BiVO}_4$  showed higher photocurrent generation than  $\text{BiVO}_4/\text{Nb}_2\text{O}_5$ , suggesting that the presence of  $\text{Nb}_2\text{O}_5$  hindered efficient hole transfer. However, the advantage of the  $\text{Nb}_2\text{O}_5$  layer was revealed by the  $J$ - $t$  measurements. The  $J$ - $t$  plot of  $\text{BiVO}_4$  at 0.7 V vs RHE showed that the photocurrent of  $\text{BiVO}_4$  increased gradually for the initial 2 h and then decreased to around  $0.4 \text{ mA}/\text{cm}^2$  at 12 h (Figure 3b). This behavior suggests that the initial photocurrent of  $\text{BiVO}_4$  was partly from photocorrosion, and that the initial photocurrent increase was due to the increase in surface area of  $\text{BiVO}_4$  caused by photocorrosion-induced dissolution of  $\text{BiVO}_4$ . As more dissolution of  $\text{BiVO}_4$  occurred, it inherently

decreased photon absorption by  $\text{BiVO}_4$ . Also, due to numerous recombination sites generated on the disintegrated  $\text{BiVO}_4$  surface, an increasing fraction of surface-reaching holes was lost to surface recombination. As a result, the photocurrent of  $\text{BiVO}_4$  could not be sustained and decreased over time. Indeed, the postanalysis of  $\text{BiVO}_4$  using XRD and SEM after the 12 h-long  $J$ - $t$  plot measurement showed a considerable loss of  $\text{BiVO}_4$  by its anodic photocorrosion (Figure 3c,d).

In contrast,  $\text{BiVO}_4/\text{Nb}_2\text{O}_5$  showed a gradual increase in photocurrent during the first 4 h but the increased photocurrent was stably maintained for the next 8 h (Figure 3b). The postanalysis of  $\text{BiVO}_4/\text{Nb}_2\text{O}_5$  using XRD after the 12 h-long  $J$ - $t$  measurement showed no notable changes in the XRD peak intensity of  $\text{BiVO}_4$  (Figure 3c). Also, the SEM image of  $\text{BiVO}_4/\text{Nb}_2\text{O}_5$  after the  $J$ - $t$  measurement shows no change in the photoanode morphology (Figure 3e). These results confirm that  $\text{Nb}_2\text{O}_5$  can effectively suppress anodic photocorrosion of  $\text{BiVO}_4$ . These results also mean that the initial photocurrent increase was not due to photocorrosion but due to some activation process of the  $\text{Nb}_2\text{O}_5$  layer, which helped enhance POER of  $\text{BiVO}_4/\text{Nb}_2\text{O}_5$ . The enhanced POER of  $\text{BiVO}_4/\text{Nb}_2\text{O}_5$  after the  $J$ - $t$  measurement was also shown in the comparison of  $J$ - $V$  plots before and after the  $J$ - $t$  measurement (Figure S3).

To better understand the effects of this activation process, we also compared photocurrents for sulfite oxidation and dark OER performances before and after the 12 h-long  $J$ - $t$  measurement (Figure S3). Sulfite is an excellent hole scavenger and all surface-reaching holes can contribute to photocurrent generation for sulfite oxidation.<sup>24</sup> Thus, comparing photocurrents for sulfite oxidation can reveal the effect of the activation process on the number of surface-reaching holes. On the other hand, comparing dark OER performances can reveal the effect of the activation process on the OER catalytic ability.

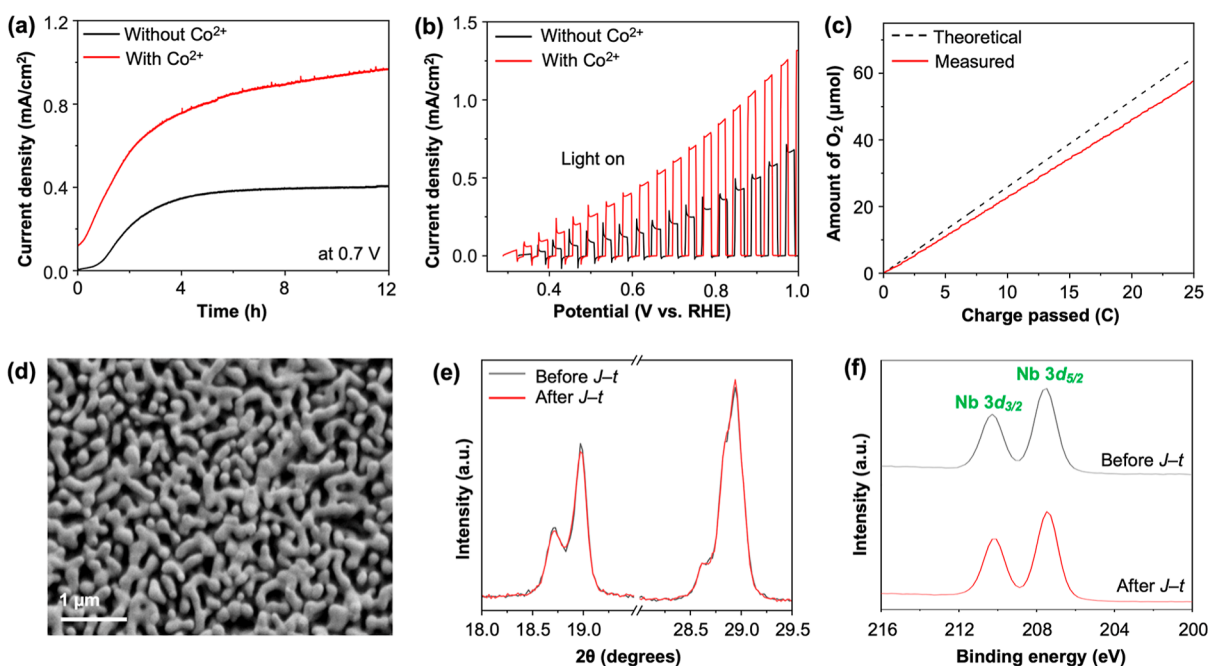


**Figure 4.** POER of  $\text{BiVO}_4/\text{Nb}_2\text{O}_5$  with 20 mM  $\text{Co}^{2+}$ . (a)  $J-t$  plots at 0.7 V vs RHE and (b)  $J-V$  plots of  $\text{BiVO}_4/\text{Nb}_2\text{O}_5$  obtained in 0.1 M  $\text{HNO}_3$  under AM 1.5G illumination ( $100 \text{ mW}/\text{cm}^2$ ) with (red) and without (black)  $\text{Co}^{2+}$ . The  $J-V$  plots were measured after the  $J-t$  plot measurements shown in (a). (c) Theoretical (black dotted line) and detected (red solid line)  $\text{O}_2$  produced during the  $J-t$  measurement with  $\text{Co}^{2+}$  at 0.7 V vs RHE. (d) SEM image, (e) XRD peaks, and (f) Nb 3d XPS spectra of  $\text{BiVO}_4/\text{Nb}_2\text{O}_5$  after the  $J-t$  measurement with  $\text{Co}^{2+}$ . Gray traces in (e,f) are measured before the  $J-t$  measurement.

Our results showed that the activation process helped improve both the number of holes reaching the surface and the OER catalytic ability (Figure S3a,b). However, no changes in the crystallinity and oxidation state of  $\text{Nb}_2\text{O}_5$  were detected by TEM and XPS analyses after the activation process (Figure S3c,d), which means that the improvements by the activation process were achieved through subtle atomic rearrangements at the  $\text{BiVO}_4/\text{Nb}_2\text{O}_5$  junction, within the  $\text{Nb}_2\text{O}_5$  layer, and on the  $\text{Nb}_2\text{O}_5$  surface without involving long-range ordering or composition change in  $\text{Nb}_2\text{O}_5$ .

We note that the results of  $\text{BiVO}_4/\text{Nb}_2\text{O}_5$  in Figure 3 are particularly remarkable since no OER catalyst was used in this experiment. Without a proper OER catalyst, more holes can accumulate at the surface, increasing the rate of photocorrosion. The fact that  $\text{Nb}_2\text{O}_5$  was able to suppress photocorrosion of  $\text{BiVO}_4$ , even when an OER catalyst was not present, suggests that  $\text{Nb}_2\text{O}_5$  offers excellent structural rigidity at the  $\text{BiVO}_4/\text{Nb}_2\text{O}_5$  interface, making the surface atomic reorganization of  $\text{BiVO}_4$  needed for photocorrosion extremely difficult. This makes the rate of photocorrosion slower than the rates of the OER and surface recombination, thus effectively suppressing the photocorrosion of  $\text{BiVO}_4$ . The  $J-V$  plot of  $\text{BiVO}_4/\text{Nb}_2\text{O}_5$  was measured again after the  $J-t$  measurement (Figure 3a, red), and it showed a significantly enhanced photocurrent compared to the initial  $J-V$  plot (Figure 3a, black) because  $\text{BiVO}_4/\text{Nb}_2\text{O}_5$  was fully activated during the  $J-t$  measurement. In contrast, the  $J-V$  plot of  $\text{BiVO}_4$  measured again after the  $J-t$  measurement showed negligible photocurrent (Figure S4).

#### POER of $\text{BiVO}_4/\text{Nb}_2\text{O}_5$ with $\text{Co}^{2+}$ as an OER Catalyst.

Next, we combine the  $\text{BiVO}_4/\text{Nb}_2\text{O}_5$  photoanode with an OER catalyst so that a greater portion of the surface-reaching holes can be used for the POER instead of surface recombination. Among various non-noble metal-based OER

electrocatalysts, Co-based catalysts have shown notable catalytic activities in acidic solutions.<sup>12,26,27</sup> However, despite many improvements, the dissolution loss of Co remains a significant concern.<sup>12</sup>

In our experiment, the POER of  $\text{BiVO}_4/\text{Nb}_2\text{O}_5$  was performed in 0.1 M  $\text{HNO}_3$  containing 20 mM  $\text{Co}^{2+}$  without predepositing a Co-containing OER catalyst on  $\text{Nb}_2\text{O}_5$ . It is known that  $\text{Co}^{2+}_{(\text{aq})}$  in solutions can be oxidized to less soluble  $\text{Co}^{3+}$  or  $\text{Co}^{4+}$  under anodic bias used for the OER and it can be deposited as a solid OER catalyst on the electrode surface during the OER.<sup>28,29</sup> Even if the Co catalyst is reduced back to  $\text{Co}^{2+}$  during the OER catalytic cycle and dissolves, the resulting  $\text{Co}^{2+}_{(\text{aq})}$  can be reoxidized, regenerating the solid catalyst and achieving stable OER performance.<sup>29</sup> Thus, we investigated how  $\text{Co}^{2+}_{(\text{aq})}$  can utilize holes from  $\text{BiVO}_4/\text{Nb}_2\text{O}_5$  for the OER in 0.1 M  $\text{HNO}_3$ .

The  $J-t$  plots of  $\text{BiVO}_4/\text{Nb}_2\text{O}_5$  obtained at 0.7 V vs RHE with and without  $\text{Co}^{2+}$  show that the presence of  $\text{Co}^{2+}$  increased photocurrent generation significantly. For example, at 12 h, the photocurrent density achieved with  $\text{Co}^{2+}$  was  $0.97 \text{ mA}/\text{cm}^2$ , which is around 2.5 times increase from  $0.41 \text{ mA}/\text{cm}^2$  achieved without  $\text{Co}^{2+}$  (Figure 4a). To verify that the photocurrent generated in the presence of  $\text{Co}^{2+}$  was indeed associated with the OER, we quantified photoelectrochemically produced  $\text{O}_2$  during the  $J-t$  measurement and the Faradaic efficiency for the OER was calculated to be  $>90\%$  (Figure 4c). The  $J-V$  plots obtained with and without  $\text{Co}^{2+}$  after the  $J-t$  measurements also clearly show a remarkable photocurrent increase caused by the presence of  $\text{Co}^{2+}$  over the entire potential region (Figure 4b).

After the  $J-t$  measurement, the  $\text{BiVO}_4/\text{Nb}_2\text{O}_5$  photoanode was examined by SEM, XRD, and XPS, and no noticeable changes in the surface morphology, crystallinity, and quantity of  $\text{BiVO}_4$  as well as the presence of  $\text{Nb}_2\text{O}_5$  were detected

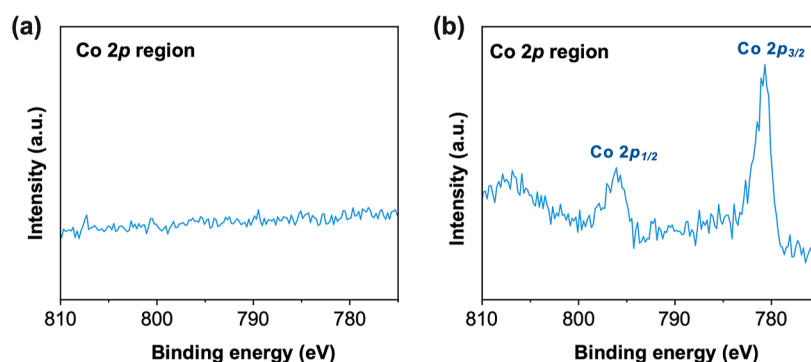


**Figure 5.** Presence of a  $\text{CoO}_x$  catalyst on  $\text{Nb}_2\text{O}_5$  after POER. Co 2p XPS spectra of (a)  $\text{BiVO}_4/\text{Nb}_2\text{O}_5$  and (b)  $\text{BiVO}_4$  obtained after the 12 h  $J-t$  measurement in the presence of  $\text{Co}^{2+}$ .

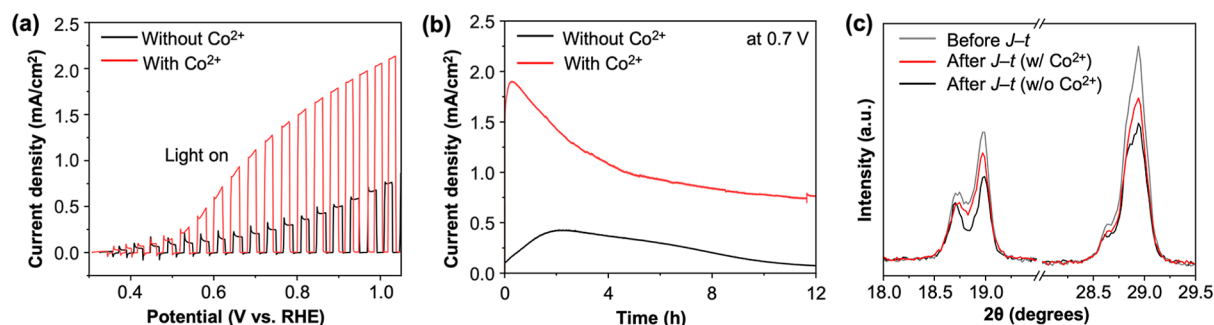


**Figure 6.** Effect of  $\text{Co}^{2+}$  on the photoelectrochemical stability of bare  $\text{BiVO}_4$  photoanodes at pH 1. (a)  $J-V$  plot and (b)  $J-t$  plot at 0.7 V vs RHE of bare  $\text{BiVO}_4$  in 0.1 M  $\text{HNO}_3$  under AM 1.5G illumination ( $100 \text{ mW}/\text{cm}^2$ ) with (red) and without (black)  $\text{Co}^{2+}$ . (c) XRD peaks of  $\text{BiVO}_4$  after the  $J-t$  measurement. Gray trace shows the XRD peaks of pristine  $\text{BiVO}_4$ .

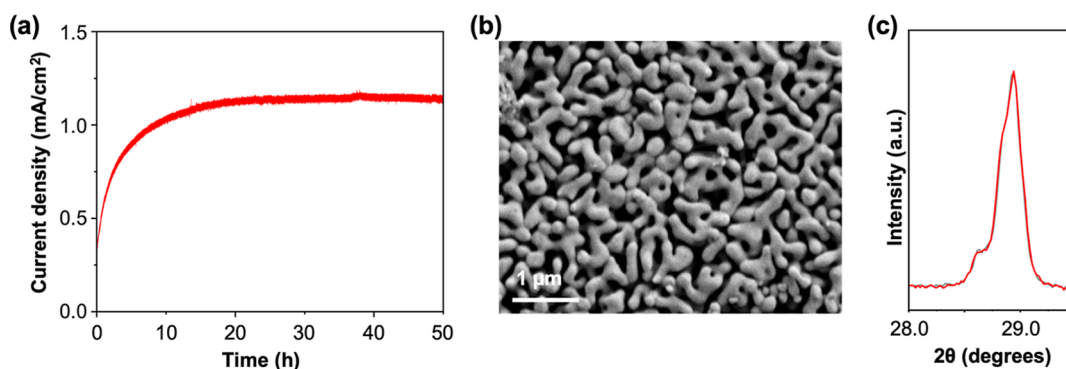


**Figure 7.** A longer-term stability of  $\text{BiVO}_4/\text{Nb}_2\text{O}_5$  for POER with  $\text{Co}^{2+}$  at pH 1. (a)  $J-t$  measurement at 0.7 V vs RHE in 0.1 M  $\text{HNO}_3$  under AM 1.5G illumination ( $100 \text{ mW}/\text{cm}^2$ ). (b) SEM image and (c) XRD result of  $\text{BiVO}_4/\text{Nb}_2\text{O}_5$  after the  $J-t$  measurement. Gray trace shows the XRD peak of pristine  $\text{BiVO}_4$ .

(Figure 4d–f). An interesting discovery from the post  $J-t$  analysis of  $\text{BiVO}_4/\text{Nb}_2\text{O}_5$  is that there was no indication that  $\text{Co}^{2+}$  was deposited as a solid OER catalyst (i.e.,  $\text{CoO}_x$ ) on  $\text{BiVO}_4/\text{Nb}_2\text{O}_5$  during the POER. The presence of  $\text{Co}^{2+}$  on the  $\text{BiVO}_4/\text{Nb}_2\text{O}_5$  surface was not detected even by XPS, although XPS is very sensitive to the surface composition (Figure 5a), implying that  $\text{Co}^{2+}$  in our system served as a homogeneous OER catalyst rather than a heterogeneous catalyst.

We also performed a control experiment where the POER of unprotected  $\text{BiVO}_4$  was performed with  $\text{Co}^{2+}_{(\text{aq})}$ . The  $J-V$  and  $J-t$  plots of  $\text{BiVO}_4$  with  $\text{Co}^{2+}$  showed a considerable increase in photocurrent generation when  $\text{Co}^{2+}$  was present, as  $\text{Co}^{2+}$  helped  $\text{BiVO}_4$  to consume a higher portion of surface-reaching holes for the POER (Figure 6a,b), which should decrease the portion of surface-reaching holes consumed for photo-

corrosion. Indeed, the XRD (Figure 6c) and SEM results (Figure S5) of unprotected  $\text{BiVO}_4$  after the  $J-t$  measurement with  $\text{Co}^{2+}$  showed that the photocorrosion-induced-dissolution of  $\text{BiVO}_4$  was decreased notably compared to the case without  $\text{Co}^{2+}$ . However,  $\text{Co}^{2+}$  alone could not protect the inherent chemical dissolution of  $\text{BiVO}_4$  in a strongly acidic solution, and the post  $J-t$  analysis showed evident destruction of  $\text{BiVO}_4$ , unlike the case of  $\text{BiVO}_4/\text{Nb}_2\text{O}_5$ . This explains why the POER of  $\text{BiVO}_4$  with  $\text{Co}^{2+}$  could not be sustained, resulting in a gradual decrease in the photocurrent over time (Figure 6b). An interesting result to note is that when unprotected  $\text{BiVO}_4$  was used with  $\text{Co}^{2+}_{(\text{aq})}$  for the POER, the post  $J-t$  XPS analysis of  $\text{BiVO}_4$  showed a significant amount of  $\text{Co}^{3+}$  present on the  $\text{BiVO}_4$  surface (Figure 5b). This means that  $\text{Co}^{2+}_{(\text{aq})}$  serving as a homogeneous OER catalyst is unique to the  $\text{BiVO}_4/\text{Nb}_2\text{O}_5$

surface, and that the Nb<sub>2</sub>O<sub>5</sub> surface is particularly inert toward the deposition of CoO<sub>x</sub> as a solid catalyst on its surface.

Finally, we examined the longer-term stability of BiVO<sub>4</sub>/Nb<sub>2</sub>O<sub>5</sub> with Co<sup>2+</sup> over 50 h in 0.1 M HNO<sub>3</sub>. After an initial activation period, the photocurrent density of BiVO<sub>4</sub>/Nb<sub>2</sub>O<sub>5</sub> reached to 1.15 mA/cm<sup>2</sup>, which was maintained stably for the remaining time (Figure 7a). The SEM image and XRD result of BiVO<sub>4</sub>/Nb<sub>2</sub>O<sub>5</sub> after 50 h of *J*-*t* measurements still did not show any indication of chemical or photoelectrochemical degradation of BiVO<sub>4</sub> (Figure 7b,c). This level of stable POER operation of oxide-based photoanodes that are chemically unstable in strongly acidic solutions has not been demonstrated previously,<sup>30,31</sup> which testifies a remarkable protection capability of an electrodeposited Nb<sub>2</sub>O<sub>5</sub> thin layer along with its unique ability to use Co<sup>2+</sup> as a homogeneous OER catalyst.

## CONCLUSIONS

In this study, we demonstrated a conformal coating of Nb<sub>2</sub>O<sub>5</sub> on a morphologically complex nanoporous BiVO<sub>4</sub> photoanode using electrodeposition to use the resulting Nb<sub>2</sub>O<sub>5</sub> layer as a protection layer to operate BiVO<sub>4</sub> photoanodes in a strongly acidic solution. The resulting BiVO<sub>4</sub>/Nb<sub>2</sub>O<sub>5</sub> electrode showed an excellent resistance against chemical dissolution of BiVO<sub>4</sub> in 0.1 M HNO<sub>3</sub> (pH 1) for 3 weeks, which confirmed the uniformity and pinhole-free nature of the electrodeposited Nb<sub>2</sub>O<sub>5</sub> layer as well as the chemical stability of a thin, amorphous Nb<sub>2</sub>O<sub>5</sub> layer in 0.1 M HNO<sub>3</sub>. When the BiVO<sub>4</sub>/Nb<sub>2</sub>O<sub>5</sub> photoanode was tested for POER, the presence of Nb<sub>2</sub>O<sub>5</sub> suppressed anodic photocorrosion of BiVO<sub>4</sub> even when no OER catalyst was used and Nb<sub>2</sub>O<sub>5</sub> is not particularly catalytic for OER. This result revealed remarkable chemical and structural robustness of Nb<sub>2</sub>O<sub>5</sub>, not allowing for atomic reorganization at the BiVO<sub>4</sub>/Nb<sub>2</sub>O<sub>5</sub> interface that needs to be coupled for the holes to photo-oxidize the BiVO<sub>4</sub> surface. This effectively decreased the rate of photocorrosion compared to the rates of OER and surface electron–hole recombination, thus kinetically preventing the consumption of surface holes for photocorrosion. When we added Co<sup>2+</sup> ions to the electrolyte, Co<sup>2+</sup><sub>(aq)</sub> served as a homogeneous OER catalyst and enhanced the POER of BiVO<sub>4</sub>/Nb<sub>2</sub>O<sub>5</sub>. The use of Co<sup>2+</sup><sub>(aq)</sub> as a homogeneous OER catalyst eliminated the need to predeposit an OER catalyst on Nb<sub>2</sub>O<sub>5</sub> as well as the concern of losing the heterogeneous OER catalyst during acidic POER due to catalyst instability. We found that when unprotected BiVO<sub>4</sub> was used with Co<sup>2+</sup><sub>(aq)</sub>, Co<sup>2+</sup> was deposited as a Co<sup>3+</sup>-containing catalyst on BiVO<sub>4</sub>, suggesting that the use of Co<sup>2+</sup><sub>(aq)</sub> as a homogeneous OER catalyst is unique on the Nb<sub>2</sub>O<sub>5</sub> surface due to the inertness of the Nb<sub>2</sub>O<sub>5</sub> surface for CoO<sub>x</sub> deposition. This study, which demonstrated stable POER of BiVO<sub>4</sub> at pH 1, revealed multiple advantages of using Nb<sub>2</sub>O<sub>5</sub> as a protection layer, which may be used to protect other photoelectrodes.

## ASSOCIATED CONTENT

### Supporting Information

The Supporting Information is available free of charge at <https://pubs.acs.org/doi/10.1021/jacs.5c11785>.

Results obtained with a thinner (~5 nm thick) Nb<sub>2</sub>O<sub>5</sub> layer, the XRD pattern of BiVO<sub>4</sub>/Nb<sub>2</sub>O<sub>5</sub>, results showing the effect of the activation process of Nb<sub>2</sub>O<sub>5</sub> on photoelectrochemical sulfite oxidation and OER in

the dark, additional results showing the performances of unprotected BiVO<sub>4</sub> (PDF)

## AUTHOR INFORMATION

### Corresponding Author

Kyoung-Shin Choi – Department of Chemistry, University of Wisconsin–Madison, Madison, Wisconsin 53706, United States; [orcid.org/0000-0003-1945-8794](https://orcid.org/0000-0003-1945-8794); Email: [kschoi@chem.wisc.edu](mailto:kschoi@chem.wisc.edu)

### Authors

Daye Seo – Department of Chemistry, University of Wisconsin–Madison, Madison, Wisconsin 53706, United States

Dae Han Wi – Department of Chemistry, University of Wisconsin–Madison, Madison, Wisconsin 53706, United States; Department of Chemistry, Chungnam National University, Daejeon 34134, Republic of Korea; [orcid.org/0000-0002-2807-4541](https://orcid.org/0000-0002-2807-4541)

Complete contact information is available at: <https://pubs.acs.org/10.1021/jacs.5c11785>

### Author Contributions

<sup>§</sup>D.S. and D.H.W. contributed equally to this work.

### Notes

The authors declare no competing financial interest.

## ACKNOWLEDGMENTS

The experimental work was supported by the Division of Chemical Sciences, Geosciences, and Biosciences, Office of Basic Energy Sciences of the U.S. Department of Energy through Grant DE-SC0024211.

## REFERENCES

- Li, J. Oxygen Evolution Reaction in Energy Conversion and Storage: Design Strategies Under and Beyond the Energy Scaling Relationship. *Nano-Micro Lett.* **2022**, *14*, 112.
- Segev, G.; Kibsgaard, J.; Hahn, C.; Xu, Z. J.; Cheng, W.-H.; Deutsch, T. G.; Xiang, C.; Zhang, J. Z.; Hammarström, L.; Nocera, D. G.; Weber, A. Z.; Agbo, P.; Hisatomi, T.; Osterloh, F. E.; Domen, K.; Abdi, F. F.; Haussener, S.; Miller, D. J.; Ardo, S.; McIntyre, P. C.; Hannappel, T.; Hu, S.; Atwater, H.; Gregoire, J. M.; Ertem, M. Z.; Sharp, I. D.; Choi, K.-S.; Lee, J. S.; Ishitani, O.; Ager, J. W.; Prabhakar, R. R.; Bell, A. T.; Boettcher, S. W.; Vincent, K.; Takane, K.; Artero, V.; Napier, R.; Cuenya, B. R.; Koper, M. T. M.; Van De Krol, R.; Houle, F. The 2022 Solar Fuels Roadmap. *J. Phys. D Appl. Phys.* **2022**, *55* (32), 323003.
- Chen, F.-Y.; Elgazzar, A.; Pecaut, S.; Qiu, C.; Feng, Y.; Ashokkumar, S.; Yu, Z.; Sellers, C.; Hao, S.; Zhu, P.; Wang, H. Electrochemical Nitrate Reduction to Ammonia with Cation Shuttling in a Solid Electrolyte Reactor. *Nat. Catal.* **2024**, *7* (9), 1032–1043.
- Roylance, J. J.; Kim, T. W.; Choi, K.-S. Efficient and Selective Electrochemical and Photoelectrochemical Reduction of 5-Hydroxymethylfurfural to 2,5-Bis(Hydroxymethyl)Furan Using Water as the Hydrogen Source. *ACS Catal.* **2016**, *6* (3), 1840–1847.
- Ledezma-Yanez, I.; Wallace, W. D. Z.; Sebastián-Pascual, P.; Climent, V.; Feliu, J. M.; Koper, M. T. M. Interfacial Water Reorganization as a pH-Dependent Descriptor of the Hydrogen Evolution Rate on Platinum Electrodes. *Nat. Energy* **2017**, *2*, 17031.
- Sheng, W.; Gasteiger, H. A.; Shao-Horn, Y. Hydrogen Oxidation and Evolution Reaction Kinetics on Platinum: Acid vs Alkaline Electrolytes. *J. Electrochem. Soc.* **2010**, *157* (11), B1529.
- Huang, J. E.; Li, F.; Ozden, A.; Sedighian Rasouli, A.; García de Arquer, F. P.; Liu, S.; Zhang, S.; Luo, M.; Wang, X.; Lum, Y.; Xu, Y.; Bertens, K.; Miao, R. K.; Dinh, C.-T.; Sinton, D.; Sargent, E. H. CO<sub>2</sub>

Electrolysis to Multicarbon Products in Strong Acid. *Science* **2021**, 372 (6546), 1074–1078.

(8) Dutta, N.; Peter, S. C. Electrochemical CO<sub>2</sub> Reduction in Acidic Media: A Perspective. *J. Am. Chem. Soc.* **2025**, 147 (11), 9019–9036.

(9) Yuan, X.; Lee, K.; Bender, M. T.; Schmidt, J. R.; Choi, K.-S. Mechanistic Differences between Electrochemical Hydrogenation and Hydrogenolysis of 5-Hydroxymethylfurfural and Their pH Dependence. *ChemSusChem* **2022**, 15 (17), No. e202200952.

(10) Yuan, X.; Lee, K.; Eisenberg, J. B.; Schmidt, J. R.; Choi, K.-S. Selective Deoxygenation of Biomass-Derived Carbonyl Compounds on Zn via Electrochemical Clemmensen Reduction. *Nat. Catal.* **2024**, 7, 43–54.

(11) Huang, J.; Clark, A. H.; Hales, N.; Crossley, K.; Guehl, J.; Skoupy, R.; Schmidt, T. J.; Fabbri, E. Oxidation of Interfacial Cobalt Controls the pH Dependence of the Oxygen Evolution Reaction. *Nat. Chem.* **2025**, 17, 856–864.

(12) Mondschein, J. S.; Callejas, J. F.; Read, C. G.; Chen, J. Y. C.; Holder, C. F.; Badding, C. K.; Schaak, R. E. Crystalline Cobalt Oxide Films for Sustained Electrocatalytic Oxygen Evolution under Strongly Acidic Conditions. *Chem. Mater.* **2017**, 29 (3), 950–957.

(13) Li, A.; Ooka, H.; Bonnet, N.; Hayashi, T.; Sun, Y.; Jiang, Q.; Li, C.; Han, H.; Nakamura, R. Stable Potential Windows for Long-Term Electrocatalysis by Manganese Oxides Under Acidic Conditions. *Angew. Chem., Int. Ed.* **2019**, 58 (15), 5054–5058.

(14) Walter, M. G.; Warren, E. L.; McKone, J. R.; Boettcher, S. W.; Mi, Q.; Santori, E. A.; Lewis, N. S. Solar Water Splitting Cells. *Chem. Rev.* **2010**, 110, 6446–6473.

(15) Park, Y.; McDonald, K. J.; Choi, K.-S. Progress in Bismuth Vanadate Photoanodes for Use in Solar Water Oxidation. *Chem. Soc. Rev.* **2013**, 42 (6), 2321–2337.

(16) Kim, T. W.; Choi, K.-S. Nanoporous BiVO<sub>4</sub> Photoanodes with Dual-Layer Oxygen Evolution Catalysts for Solar Water Splitting. *Science* **2014**, 343 (6174), 990–994.

(17) Lee, D. K.; Choi, K.-S. Enhancing Long-Term Photostability of BiVO<sub>4</sub> Photoanodes for Solar Water Splitting by Tuning Electrolyte Composition. *Nat. Energy* **2018**, 3, 53–60.

(18) Kuang, Y.; Jia, Q.; Ma, G.; Hisatomi, T.; Minegishi, T.; Nishiyama, H.; Nakabayashi, M.; Shibata, N.; Yamada, T.; Kudo, A.; Domen, K. Ultrastable Low-Bias Water Splitting Photoanodes via Photocorrosion Inhibition and in Situ Catalyst Regeneration. *Nat. Energy* **2017**, 2 (1), 16191.

(19) Lee, D.; Kvit, A.; Choi, K.-S. Enabling Solar Water Oxidation by BiVO<sub>4</sub> Photoanodes in Basic Media. *Chem. Mater.* **2018**, 30 (14), 4704–4712.

(20) Bae, S.; Moehl, T.; Service, E.; Kim, M.; Adams, P.; Wang, Z.; Choi, Y.; Ryu, J.; Tilley, S. D. A Hole-Selective Hybrid TiO<sub>2</sub> Layer for Stable and Low-Cost Photoanodes in Solar Water Oxidation. *Nat. Commun.* **2024**, 15 (1), 9439.

(21) Kim, T. W.; Ping, Y.; Galli, G. A.; Choi, K.-S. Simultaneous Enhancements in Photon Absorption and Charge Transport of Bismuth Vanadate Photoanodes for Solar Water Splitting. *Nat. Commun.* **2015**, 6, 8769.

(22) Pourbaix, M. *Atlas of Electrochemical Equilibria in Aqueous Solutions*, 2nd ed.; National Association of Corrosion Engineers, 1974.

(23) Arunachalam, M.; Kanase, R. S.; Badiger, J. G.; Sayed, S. A.; Ahn, K.-S.; Ha, J.-S.; Ryu, S.-W.; Kang, S. H. Durable Bias-Free Solar Water-Splitting Cell Composed of n<sup>+</sup>+p-Si/Nb<sub>2</sub>O<sub>5</sub>/NiPt Photocathode and W:BiVO<sub>4</sub>/NiCo(O-OH)<sub>2</sub> Photoanode. *Chem. Eng. J.* **2023**, 474, 145262.

(24) Kang, D.; Kim, T. W.; Kubota, S. R.; Cardiel, A. C.; Cha, H. G.; Choi, K.-S. Electrochemical synthesis of photoelectrodes and catalysts for use in solar water splitting. *Chem. Rev.* **2015**, 115 (23), 12839–12887.

(25) McDonald, K. J.; Choi, K.-S. A New Electrochemical Synthesis Route for a BiOI Electrode and Its Conversion to a Highly Efficient Porous BiVO<sub>4</sub> Photoanode for Solar Water Oxidation. *Energy Environ. Sci.* **2012**, 5 (9), 8553–8557.

(26) Li, A.; Kong, S.; Guo, C.; Ooka, H.; Adachi, K.; Hashizume, D.; Jiang, Q.; Han, H.; Xiao, J.; Nakamura, R. Enhancing the Stability of

Cobalt Spinel Oxide towards Sustainable Oxygen Evolution in Acid. *Nat. Catal.* **2022**, 5, 109–118.

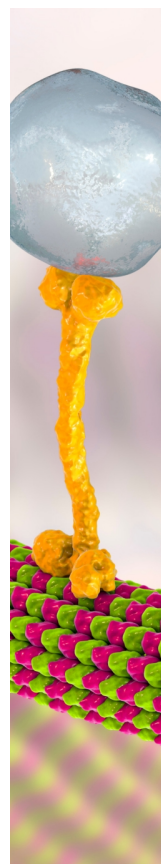
(27) Chong, L.; Gao, G.; Wen, J.; Li, H.; Xu, H.; Green, Z.; Sugar, J. D.; Kropf, A. J.; Xu, W.; Lin, X.-M.; Xu, H.; Wang, L.-W.; Liu, D.-J. La- and Mn-Doped Cobalt Spinel Oxygen Evolution Catalyst for Proton Exchange Membrane Electrolysis. *Science* **2023**, 380 (6645), 609–616.

(28) Chatti, M.; Gardiner, J. L.; Fournier, M.; Johannessen, B.; Williams, T.; Gengenbach, T. R.; Pai, N.; Nguyen, C.; MacFarlane, D. R.; Hocking, R. K.; Simonov, A. N. Intrinsically Stable in Situ Generated Electrocatalyst for Long-Term Oxidation of Acidic Water at up to 80 °C. *Nat. Catal.* **2019**, 2, 457–465.

(29) Thorarindottir, A. E.; Veroneau, S. S.; Nocera, D. G. Self-Healing Oxygen Evolution Catalysts. *Nat. Commun.* **2022**, 13, 1243.

(30) Tang, P.-Y.; Han, L.-J.; Hegner, F. S.; Paciok, P.; Biset-Peiró, M.; Du, H.-C.; Wei, X.-K.; Jin, L.; Xie, H.-B.; Shi, Q.; Andreu, T.; Lira-Cantú, M.; Heggen, M.; Dunin-Borkowski, R. E.; López, N.; Galán-Mascarós, J. R.; Morante, J. R.; Arbiol, J. Boosting Photoelectrochemical Water Oxidation of Hematite in Acidic Electrolytes by Surface State Modification. *Adv. Energy Mater.* **2019**, 9 (34), 1901836.

(31) Li, T.-T.; Cui, J.-Y.; Xu, M.; Song, K.; Yin, Z.-H.; Meng, C.; Liu, H.; Wang, J.-J. Efficient Acidic Photoelectrochemical Water Splitting Enabled by Ru Single Atoms Anchored on Hematite Photoanodes. *Nano Lett.* **2024**, 24 (3), 958–965.



CAS BIOFINDER DISCOVERY PLATFORM™

## BRIDGE BIOLOGY AND CHEMISTRY FOR FASTER ANSWERS

Analyze target relationships,  
compound effects, and disease  
pathways

Explore the platform

**CAS**  
A Division of the  
American Chemical Society